Second gradient vs. hyper-pre-stress for surface relaxation in diamond-like structures

Alexandre Danescu

Lyon Institute of Nanotechnology, Ecole Centrale de Lyon, 69131 Ecully, France

Abstract

In this paper, based on the discrete valence force field model for diamond-like crystals we construct and compare predictions of two models with cubic symmetry containing an intrinsic internal length. The first model is constructed using lattice dynamics and the classical polynomial approximation of the acoustic branches near the Γ point. We show that the second-gradient continuum approximation obtained in this way leads to unphysically small internal lengths, enforcing a result obtained previously recently in [1]. The second model follows a line studied in the one-dimensional context in [2]. It takes into account incompatible reference lengths in the discrete setting and is able to model both cohesion, surface energy and defects. We study the ground state of an infinite lattice and we conclude that as expected, for parameters in the range of interest, a boundary-layer effect occur. We explore numerically using the second model : (a) the average lattice parameter of bulk-like, plate-like and beam-like nano-structures and (b) we predict lattice parameter variations as a function of porosity in porous silicon. We conclude that the anisotropic three-dimensional model with hyper-pre-stress provides a realistic model for mechanics of nano-structures.

Keywords: dispersive corrections of elasticity – hyper-pre-stress – surface relaxation – elastic constants

---

Email address: `alexandre.danescu@ec-lyon.fr` (Alexandre Danescu)

Preprint submitted to Elsevier *June 24, 2011*

Contents

1. Introduction

It is well admitted that for objects with at least one very small characteristic length (ultra-thin films, nano-wires, nano-tubes, etc.) the macroscopic properties are governed by the competition between bulk and surface effects and thus may deviate significantly from the bulk properties. The review presented in [3] shows several generic experimental facts : for instance, $\langle 100 \rangle$ oriented Ag nano-wires exhibit dramatic increase of the Young modulus, while for the $\langle 110 \rangle$ oriented Si nano-wires a softening phenomena occurs. Most of these experimental facts can be explained using atomistic calculations but, following the conclusion in [3] there is still a large gap between computational predictions and experimental measurements of the Young modulus both for metallic and semiconductor nano-wires, and more generally for nano-structures.

From a theoretical point of view, experimental evidence about the dependence of the elastic moduli on the specimen size, commonly called *size effects*, requires at the continuum level, a theory containing at least an *intrinsic internal length scale*. The simplest generalization of the classical linear elasticity that includes an internal length is to include the second-gradient of the displacement field in the expression of the elastic energy density ([4] [5], [6]), [7]. Theoretical predictions of the resulting theory allow the identification of higher-order constants from a phenomenological basis and were largely discussed in the recent years (see for example [8] and references within). Main applications discuss mainly isotropic materials[9], when the coupling between the first and the second gradient of the displacement field vanishes, leading to a non-local model including five new material parameters (see also [10], [11] for strain gradients in plasticity). Generally, including second-gradients in the continuum description leads to some *boundary layers effects* associated with manifestations of surface and/or interfaces effects.

In a recent work [1], following a line previously developed in [12], an atomistic approach based on density functional theory and molecular dynamics was used in order to determine strain-gradient elasticity constants. The second-gradient theory obtained in this way posses higher-order material parameters which can be obtained from the discrete model. From this perspective, the linear elasticity theory is *a first-order approximation* of the discrete model, while the second-gradient theory is a *second-order approximation*. From an analytical point of view, for very simple discrete models we face an apparent paradox : the material parameters of the second-gradient theory will depend on the first-order elasticities and some geometric characteristics of the discrete structure, as the lattice parameter. Along this line [1] show that, for a large class of materials including both metals and semi-conductors, the second-order effects computed manifest only at *unphysical small sizes*.

An interesting theoretical argument able to include an internal length in the discrete setting was presented in [2]. A detailed analysis of the mechanical response of the one dimensional chain including NN and NNN interactions *with incompatible reference lengths* shows that, in the generic case, *boundary layers occur*. However, in contrast with the continuum setting, in this case the reference configuration of the chain is non-trivial so, as a consequence, at very small scales, the elasticity of the chain may deviate significantly from the classical predictions of the homogenization theory. This is in a certain sense expected since elasticity reflects only material behavior at very large scales with respect to the inter-particle distance.

In this paper, motivated by the experimental evidence of size-dependent lattice parameter in nano-porous silicon, we explore the two lines presented above for materials with diamond-like structure. The starting point is the discrete valence force field (VFF) model that fits remarkably well the bulk elasticity of group IV elements in the diamond-like structure. Using lattice dynamics we derive explicitly the second-order approximation, i.e. the continuum second-gradient approximation of the discrete model following the method of [12]. The key point on this line is the approximation of the dispersion relations near the Γ point in the multi-dimensional case with cubic symmetry. The analytical results obtained on this line complete and enforces the conclusions obtained by [1]. We show that the length-scales obtained are too small to predict correctly the size-dependent lattice parameter observed in nano-porous silicon, which is a seriously drawback of the second-gradient theory, already evidenced using a different approach in [1].

Back to the discrete setting and following the ideas in [2] we explore a second alternative that includes in the VFF model *incompatible reference lengths*. On this line we construct a discrete model for crystals with diamond lattice structure able to predict both (a) the variations of the lattice parameter during the porosification and (b) the correct macroscopic elastic constants. The key point in the construction of a model with hyper-pre-stress is to add a specific null-lagrangian to the discrete model and we evidence the role of the ground state in the choice of material parameters. The analytical complexity of the resulting three-dimensional discrete model is prohibitive for a complete qualitative study comparable with that of the one-dimensional chain [2] but, using numerical simulations, we evidence several size effects induced by the presence of the incompatible reference lengths acting on NN and angular interactions. The numerical study of the average lattice parameter of beam-like, plate-like and bulk-like structures of Si evidence enhanced relaxation of beam-like structure with respect to plate-like structures and plate-like structures with respect to bulk like structures. We fit the single new material parameter of the model using available Raman spectroscopy data obtained for porous bulk silicon in a range of moderate porosities.

2. Discrete models for diamond-like structures

2.1. An overview

In a fundamental paper on discrete interactions in covalent crystals, Tersoff [13] divides interaction potentials in two major groups: the first one contains the *pair interaction potentials* (Lennard-Jones, Morse, etc.) which apply to arbitrary configurations but give poor results for strong covalent bonds. In this direction, the pioneering work of Born was extended by Hermann [14] up to fifth-shell in an attempt to fit both elastic moduli and the phonon dispersion data for silicon. The second group of potentials, intended to describe small distorsions from a ground state includes three-body potentials and the most famous example is the simplest valence force field model of Keating [15]. Formally, for a system containing N particles the total interaction energy can be expanded in a formal Taylor series as

$$W = \sum_{1 \leq i \leq N} V_1(\boldsymbol{r}_i) + \sum_{1 \leq i < j \leq N} V_2(\boldsymbol{r}_i, \boldsymbol{r}_j) + \sum_{1 \leq i < j < k \leq N} V_3(\boldsymbol{r}_i, \boldsymbol{r}_j, \boldsymbol{r}_k) + \dots \tag{1}$$

Models accounting only for pair interactions (Lennard-Jones, Morse, etc.) consider only approximations accounting for the first two terms, usually including a cut-off radius. Models in the second group include *at least* the third term and are able to provide a fairly good description of the elastic properties of diamond-like structures of group IV elements : C, Si, Ge. We note here that accounting for NNN interactions (or more longer range pair(interactions) is obviously not equivalent to accounting for three-body terms. Moreover, the rôle of angular interactions can be evidenced only in multidimensional setting.

Among the models designed to extend the models of Born and Keating we cite here the most common :

(i) **The Stillinger-Weber model :** (which falls in the second group) for which the interaction energy is given by

$$W = \sum_{i,j} V_2(|\boldsymbol{r}_j - \boldsymbol{r}_i|) + \sum_{i,j,k} \lambda e^{\gamma \left[\frac{1}{r_{ij} - a} + \frac{1}{r_{ik} - a} \right]} (\cos\theta_{ijk} + 1/3)^2 \tag{2}$$

where λ and γ are material constants θ_{ijk} is the angle between $\boldsymbol{r}_{ij}$ and $\boldsymbol{r}_{ik}$ and a is the lattice parameter. The model includes nonlinearities able to give a fairly realistic description of crystalline silicon but encounter transferability problems (i.e., is unable to cover non-tetrahedral polytypes).

(ii) **The Tersoff model :** [13] The interaction energy is assumed to have the form :

$$W = \sum_{i,j} f_c(r_{ij}) \left[A e^{-\lambda_1 r_{ij}} + B(1 + \beta^n \xi_{ij^n})^{\frac{1}{2n}} e^{-\lambda_2 r_{ij}} \right] \tag{3}$$

where $\xi_{ij} = \sum_{k \neq i,j} f_c(r_{ij}) \left[1 + \frac{c^2}{d^2} + \frac{c^2}{d^2 + (h - \cos\theta_{ijk})^2} \right] e^{\lambda_3^3 (r_{ij} - r_{ik})^3}$ and f_c is a cut-off function and $A, B, \lambda_1, \lambda_2, \lambda_3, \beta, n, c, d$ and h are material parameters. The model emphasize the fundamental role of the *coordination* and use only pair interactions with the bond strength depending on coordination. It covers a broad spectrum of situations but fitting to real situations is a hard task. In particular the model predicts [13] for the elastic constants of silicon : $C_{11} = 121$ GPa, $C_{12} = 86$ GPa and $C_{44} = 10$ GPa in disagreement with experimental data ([16] : $C_{11} = 165$ GPa, $C_{12} = 63$ GPa and $C_{44} = 79$ GPa).

(iii.) **The embedded atom method** model [17], [18] where

$$W = \sum_i f(\rho_i) + \sum_{i,j} V_2(r_{ij}) \tag{4}$$

and $f(\rho_i)$ is the electron density around the atom i and V_2 is a pair potential, both calibrated from quantum mechanical calculations.

Justification of the form of the cohesive energy potentials from band theory [19] may motivate both angular terms in 2, [13] and pair terms giving a matrix description of an atoms local environment ([20] with applications to Si).

2.2. The valence force field model of Keating

The simplest valence force field (VFF) model of Keating [15] assumes that, in the harmonic regime near a ground state, the total elastic energy of a covalent system can be decomposed as a sum between a central and a non-central interaction energies as:

$$W = \sum_{(i,j)} w_i^j + \sum_{(i,j,k)} w_i^{jk}. \tag{5}$$

where the pair potential w_i^j and the three-body potential w_i^{jk} are given, respectively, by

$$w_i^j = \frac{2A}{3a^2}((\boldsymbol{x}^j - \boldsymbol{x}^i) \cdot (\boldsymbol{x}^j - \boldsymbol{x}^i) - \frac{3a^2}{16})^2 \tag{6}$$

$$w_i^{jk} = \frac{8B}{3a^2}((\boldsymbol{x}^j - \boldsymbol{x}^i) \cdot (\boldsymbol{x}^k - \boldsymbol{x}^i) + \frac{a^2}{16})^2. \tag{7}$$

In (6) and (7) we use a for the lattice parameter and $\boldsymbol{x}^i$ for the positions of the atom i. Using $\boldsymbol{u}^i$ for the displacement of the atom i with respect to its position $\boldsymbol{X}^i$ on the reference configuration (the diamond lattice with lattice parameter a), we have

$$\boldsymbol{x}^i = \boldsymbol{X}^i + \boldsymbol{u}^i \tag{8}$$

so that $\boldsymbol{x}^j - \boldsymbol{x}^i = a\frac{\sqrt{3}}{4}\boldsymbol{n}^{ij} + (\boldsymbol{u}^j - \boldsymbol{u}^i)$.

It follows that, up to third-order terms in the displacement, the interaction energies in the VFF model have expressions given by:

$$w_i^j \simeq \frac{A}{2}\left[(\vec{u}^j - \vec{u}^i) \cdot \vec{n}^{ij}\right]^2 \tag{9}$$

and

$$w_i^{jk} \simeq \frac{B}{2}\left[(\vec{u}^j - \vec{u}^i) \cdot \vec{n}^{ki} + (\vec{u}^k - \vec{u}^i) \cdot \vec{n}^{ji}\right]^2. \tag{10}$$

where in (9) and (10) A and B are stiffnesses for, respectively, central and non-central interactions.

Thus the model with interaction energy given by

$$W = \sum_{(i,j)} \frac{A}{2}\left[(\vec{u}^j - \vec{u}^i) \cdot \vec{n}^{ij}\right]^2 + \sum_{(i,j,k)} \frac{B}{2}\left[(\vec{u}^j - \vec{u}^i) \cdot \vec{n}^{ki} + (\vec{u}^k - \vec{u}^i) \cdot \vec{n}^{ji}\right]^2. \tag{11}$$

is *the quadratic approximation of the VFF model.*

We notice first that both the VFF model and it's quadratic approximation have a trivial reference configuration which is the diamond type structure with lattice parameter a. Thus, in the regime of small strains, near the ground state of the diamond lattice with lattice parameter a, both the VFF model and it's quadratic approximation give identical results.

2.3. Macroscopic elasticity for the VFF model

The most important feature of the VFF model of Keating is it's ability to accurately describe the elasticity of diamond-like crystals. This shows that, near the ground state, the simple NN pair interactions and three-body angular interactions are the dominant terms in the expression of the elastic energy of the diamond structure. For completeness, we shall briefly present here the computation of the macroscopic elasticity predicted by the VFF model. The discrete homogenization method we use is well admitted and can be rigourously justified at the analytical level ([21], [22] under suitable hypothesis fulfilled here).

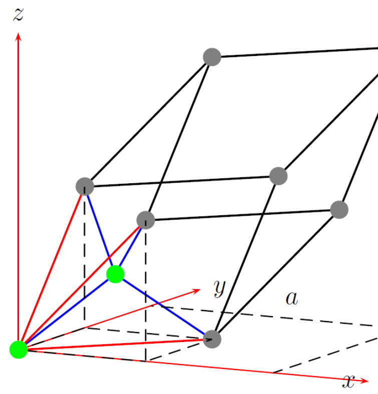

Figure 1: A unit cell of a tetrahedraly bonded structure; each unit cell contains 2 identical atoms, 4 pair-interactions and 12 angular interactions.

We consider in an infinite crystal the unit cell represented in figure 1 and containing two identical atoms. Submitted to the macroscopic strain $\boldsymbol{E}$, the individual displacements of the atoms in the cell will be given by

$$\boldsymbol{u}^1 = \boldsymbol{E}\boldsymbol{X}^1 + \tilde{\boldsymbol{u}}_1, \qquad \boldsymbol{u}^2 = \boldsymbol{E}\boldsymbol{X}^2 + \tilde{\boldsymbol{u}}_2. \tag{12}$$

Since the elastic energy is invariant with respect to translation of the cell, assuming periodicity and without loosing the generality, we can suppose that $\tilde{\boldsymbol{u}}_1 = \boldsymbol{0}$ and use $\boldsymbol{U}$ instead of $\tilde{\boldsymbol{u}}^2$. Collecting together the contributions of the 4 terms accounting for the pair interactions of a unit cell and the 12 terms accounting for three-body interactions, we obtain per unit cell

$$W = \frac{1}{24}\left[a^2(A + 12B)(E_{11}^2 + E_{22}^2 + E_{33}^2) + \right.$$

$$+2a^2(A-4B)(E_{11}E_{22}+E_{22}E_{33}+E_{11}E_{33})+4a^2(A+4B)(E_{12}^2+E_{13}^2+E_{23}^2)+$$

$$+16a(A-4B)(E_{23}U_x+E_{13}U_y+E_{12}U_z)+16(A+4B)(U_x^2+U_y^2+U_z^2)\big] \quad (13)$$

Position of the atom 2, under imposed macroscopic deformation, is provided by the minimization with respect to $\boldsymbol{U}$ in (13). This gives

$$\boldsymbol{U} = -\frac{a}{2}\frac{A-4B}{A+4B}\begin{pmatrix} E_{23} \\ E_{13} \\ E_{12} \end{pmatrix}. \quad (14)$$

and represent the local equilibrium of the lattice. Substitution of this result in (13) leads to the quadratic form

$$W_{macro.}(\boldsymbol{E}) = \frac{1}{vol(Y)}\min_{\boldsymbol{U}} W_{micro}(\boldsymbol{E},\boldsymbol{U}) =$$

$$= \frac{1}{6a(A+4B)}\big[A^2(E_{11}+E_{22}+E_{33})^2+16AB(E_{11}^2+E_{22}^2+E_{33}^2)+4(E_{12}^2+E_{13}^2++E_{23}^2)$$

$$+16B^2(3(E_{11}^2+E_{22}^2+E_{33}^2)-2(E_{11}E_{22}+E_{11}E_{33}+E_{22}E_{33}))\big] \quad (15)$$

which can be formally expressed as

$$W_{macro}(\boldsymbol{E}) = \frac{1}{2}\begin{pmatrix} C_{11} & C_{12} & C_{12} & 0 & 0 & 0 \\ C_{11} & C_{11} & C_{12} & 0 & 0 & 0 \\ C_{11} & C_{12} & C_{11} & 0 & 0 & 0 \\ 0 & 0 & 0 & C_{44} & 0 & 0 \\ 0 & 0 & 0 & 0 & C_{44} & 0 \\ 0 & 0 & 0 & 0 & 0 & C_{44} \end{pmatrix}\begin{pmatrix} E_{11} \\ E_{22} \\ E_{33} \\ 2E_{23} \\ 2E_{13} \\ 2E_{12} \end{pmatrix}\cdot\begin{pmatrix} E_{11} \\ E_{22} \\ E_{33} \\ 2E_{23} \\ 2E_{13} \\ 2E_{12} \end{pmatrix} \quad (16)$$

if

$$C_{11} = \frac{A+12B}{3a}, \qquad C_{12} = \frac{A-4B}{3a}, \qquad C_{44} = \frac{16AB}{3a(A+4B)}. \quad (17)$$

As expected, the result is the macroscopic elastic energy of a material with cubic symmetry, inherited from the (point group) symmetry of the lattice and interactions.

At a qualitative level, it is interesting to note here that the three macroscopic elasticities depend on only two microscopic parameters (stiffnesses A and B) so that the models also predict the relation

$$\frac{2C_{44}(C_{11}+C_{12})}{(C_{11}-C_{12})(C_{11}+3C_{12})}=1. \tag{18}$$

which is verified remarkably well for all group IV elements. The following table gives the values of material parameters A and B obtained using experimental data for C_{11} and C_{12}, the predicted elastic constant C_{44}, the experimental value for C_{44} from [16] and the value of the ratio in the left-hand side of (18).

	a (Å)	A (N/m)	B (N/m)	C_{44}^{th} (GPa)	C_{44}^{exp} (GPa)	LHS in (18)
C	3.567	388.1	63.87	575.9	578	1.004
Si	5.431	145.8	10.38	79.3	79.6	1.002
Ge	5.658	109.5	8.67	62.2	67.7	1.08

Table 1: Lattice parameter, material parameters A, B, predicted and experimental data for C_{44} and the value of the left-hand-side in (18) at 300K for C, Si and Ge [16].

The model (5)-(6)-(7) is unable to predict surface relaxation of nano-structures as it does not contain an internal length. Otherwise stated, the different local environment (coordination) of atoms situated far or near a free-surface in a finite domain do not affect the size of a finite structure. The reason for this is the fact that all forces acting on particles vanish simultaneously in the ground state, which is also the actual reference configuration.

Among the different methods leading to models with internal lengths we shall explore in the next section a second-gradient continuum approximation of the discrete VFF model. To this end, we follow the classical line initiated by Krumhansl [23] and exposed in detail in Kunin [24]. This procedure offers also a different perspective of the result obtained in this section.

3. Second-gradient model via lattice dynamics

This section presents the lattice dynamics for diamond structures based on the discrete VFF model of Keating and two of its continuum approximations. The basic idea is to obtain the dispersion relation and then to look for approximations of the acoustic branches near the center of the first Brillouin zone (the Γ point). As the elastic energy is invariant to translations the lower-order polynomial approximation will leads to linear elasticity with macroscopic constants described in the previous section which corresponds to quadratic polynomial approximation of the acoustic branches near the Γ point. Successive higher-order polynomial approximations will correspond to higher-order partial derivatives in the continuous setting [25] and, among this, the simplest is a second-gradient model we look for.

For the lattice dynamics calculations we shall follow the general presentation of Mielke [21].

3.1. Lattice dynamics

The diamond structure is a non-primitive lattice with 2 atoms per unit cell, further denoted by i and j. Dynamics for each atom is governed by

$$m\ddot{\mathbf{u}}^i = -\frac{\partial W}{\partial \boldsymbol{u}^i} \tag{19}$$

where the total elastic energy is the sum of central and non-central parts described by (11). Taking into account pair and three-body interactions in the the right-hand side of (19), displacement of atom i contributes to

$$\frac{\partial W}{\partial \boldsymbol{u}^i} = \sum_{j\in NN(i)} \frac{\partial W_i^j}{\partial \boldsymbol{u}^i} + \sum_{\substack{\{j,k\}\subset NN(i)\\ k\neq j}} \frac{\partial W_i^{jk}}{\partial \boldsymbol{u}^i} + \sum_{\substack{j\in NN(i)\\ k\in NN(j)\\ k\neq i}} \frac{\partial W_j^{ik}}{\partial \boldsymbol{u}^i} \tag{20}$$

where we have used $NN(i)$ for subscripts j corresponding to atoms which are near-neighbors of atom i. If we introduce $\boldsymbol{E}_i^{jk} = \boldsymbol{n}^{ij} \otimes \boldsymbol{n}^{ik}$ we obtain:

- Contribution of central forces (atom j is NN of atom i):

$$-\sum_{j\in NN(i)} \frac{\partial W_i^j}{\partial \boldsymbol{u}^i} = A \sum_{j\in NN(i)} \boldsymbol{E}_i^{jj}(\boldsymbol{u}^j - \boldsymbol{u}^i) \tag{21}$$

- Contribution of non-central forces of the type W_i^{jk} (atoms j and k are NN of atom i):

$$-\sum_{\substack{\{j,k\}\subset NN(i)\\ k\neq j}} \frac{\partial W_i^{jk}}{\partial \boldsymbol{u}^i} =$$

$$= B \sum_{\substack{\{j,k\}\subset NN(i)\\ k\neq j}} \Big[(\boldsymbol{E}_i^{jj} + \boldsymbol{E}_i^{kj})(\boldsymbol{u}^k - \boldsymbol{u}^i) + (\boldsymbol{E}_i^{kk} + \boldsymbol{E}_i^{jk})(\boldsymbol{u}^j - \boldsymbol{u}^i)\Big] \tag{22}$$

- Contribution of non-central forces of the type W_j^{ik} (atom k and i are NN of atom j):

$$-\sum_{\substack{j\in NN(i)\\ k\in NN(j)\\ k\neq i}} \frac{\partial W_j^{ik}}{\partial \boldsymbol{u}^i} = -B \sum_{\substack{j\in NN(i)\\ k\in NN(j)\\ k\neq i}} \Big[\boldsymbol{E}_j^{kk}(\boldsymbol{u}^i - \boldsymbol{u}^j) + \boldsymbol{E}_j^{ki}(\boldsymbol{u}^k - \boldsymbol{u}^j)\Big] \tag{23}$$

Since the diamond structure is a non-primite lattice, we have to distinguish in the right-hand side of (19) the contribution of particles from different FCC-sublattices. We first note that :

- In (21) and (22) subscripts i and j correspond to atoms situated in different sublattices, while k correspond to an atoms situated in the same sublattice as j;

- In (23) subscripts i and j correspond to atoms in different sublattices, while k correspond to an atom in the same sublattice as i.

Next step is to look for particular solutions in the form of progressive plane waves for each sublattice, i.e.

$$\boldsymbol{u} = \boldsymbol{U} e^{i(\boldsymbol{k}\cdot\boldsymbol{x} + \omega t)} \tag{24}$$

using $\boldsymbol{U}$ for the amplitude in one of the sublattice and $\boldsymbol{V}$ for the other.

At this point we need to describe the coordination around a fixed atom in one (of the lattices). To this end, we introduce 4 vectors $\boldsymbol{v}_1$, $\boldsymbol{v}_2$, $\boldsymbol{v}_3$ and $\boldsymbol{v}_4$ giving the positions of the four near neighbors of an atom of one of the sublattices[1]. We obviously have $\sum_{i=1}^{4} \boldsymbol{v}_i = \mathbf{0}$ so, as a consequence, the coordination around an atom of the second lattice is given by the opposite vectors. It follows that, formally, the dynamics of both sublattices are given by similar equations but their connectivity is described by the opposite vectors.

Collecting together results in (21), (22) and (23) and using (24) we obtain after simplification for one sublattice

$$\begin{aligned}
-\omega^2 m\boldsymbol{U} = \Bigg[-A \sum_{j\in NN(i)} \boldsymbol{E}_i^{jj} - B \Bigg[& \sum_{\substack{\{j,k\}\subset NN(i)\\ k\neq j}} (\boldsymbol{E}_i^{jj} + \boldsymbol{E}_i^{kj} + \boldsymbol{E}_i^{kk} + \boldsymbol{E}_i^{jk}) + \\
& + \sum_{\substack{j\in NN(i)\\ k\in NN(j)\\ k\neq i}} (\boldsymbol{E}_j^{kk} + \boldsymbol{E}_j^{ki} e^{\boldsymbol{ik}\cdot(\boldsymbol{v}_j - \boldsymbol{v}_k)}) \Bigg]\Bigg] \boldsymbol{U} + \\
+ \Bigg[A \sum_{j\in NN(i)} \boldsymbol{E}_i^{jj} e^{\boldsymbol{ik}\cdot\boldsymbol{v}_j} + B \Bigg[& \sum_{\substack{\{j,k\}\subset NN(i)\\ k\neq j}} \Big[(\boldsymbol{E}_i^{jj} + \boldsymbol{E}_i^{kj}) e^{\boldsymbol{ik}\cdot\boldsymbol{v}_k} + (\boldsymbol{E}_i^{jk} + \boldsymbol{E}_i^{kk}) e^{\boldsymbol{ik}\cdot\boldsymbol{v}_j} \Big] + \\
& + \sum_{\substack{j\in NN(i)\\ k\in NN(j)\\ k\neq i}} (\boldsymbol{E}_j^{kk} + \boldsymbol{E}_j^{ki}) e^{\boldsymbol{ik}\cdot\boldsymbol{v}_j} \Bigg]\Bigg] \boldsymbol{V} \qquad (25)
\end{aligned}$$

We shall denote by $-\mathbf{A}_{UU}$ and $-\mathbf{A}_{UV}$ respectively the factors of $\boldsymbol{U}$ and $\boldsymbol{V}$ in the above equation. We notice that, since coordination in the second lattice is obtained by changing $\boldsymbol{v}_i$ to $-\boldsymbol{v}_i$, the dynamics of the second lattice is governed by

$$\boldsymbol{A}_{UV}^{\star}\boldsymbol{U} + \boldsymbol{A}_{VV}\boldsymbol{V} - \omega^2 m\boldsymbol{V} = \mathbf{0}, \qquad (26)$$

---

[1] These vectors are represented in Figure 1 inside the unit cell.

where

$$
\begin{aligned}
\boldsymbol{A}_{VV} = \Bigg[A \sum_{j\in NN(i)} \boldsymbol{E}_i^{jj} + \\
+B \Bigg[\sum_{\substack{\{j,k\}\subset NN(i)\\ k\neq j}} (\boldsymbol{E}_i^{jj} + \boldsymbol{E}_i^{kj} + \boldsymbol{E}_i^{kk} + \boldsymbol{E}_i^{jk}) + \sum_{\substack{j\in NN(i)\\ k\in NN(j)\\ k\neq i}} (\boldsymbol{E}_j^{kk} + \boldsymbol{E}_j^{ki} e^{-i\boldsymbol{k}\cdot(\boldsymbol{v}_j-\boldsymbol{v}_k)}) \Bigg] \Bigg]
\end{aligned}
\tag{27}
$$

so that, finally, the system has the following structure

$$
\left(\boldsymbol{A}(\boldsymbol{k}) - \omega^2 m \boldsymbol{I}_{6\times 6}\right) \begin{bmatrix} \boldsymbol{U} \\ \boldsymbol{V} \end{bmatrix} = \begin{bmatrix} \boldsymbol{0} \\ \boldsymbol{0} \end{bmatrix}, \tag{28}
$$

where, $\boldsymbol{A}(\boldsymbol{k})$ denotes the dispersion matrix

$$
\boldsymbol{A}(\boldsymbol{k}) = \begin{bmatrix} \mathbf{A}_{UU} & \mathbf{A}_{UV} \\ \mathbf{A}^{\star}_{UV} & \mathbf{A}_{VV} \end{bmatrix}. \tag{29}
$$

3.2. Separation of the acoustic and optical branches

We are interested in the structure of the spectrum of $\boldsymbol{A}(\boldsymbol{k})$ near the Γ-point, i.e., $\boldsymbol{k} = \boldsymbol{0}$ which is the center of the first Brillouin zone. Invariance of the cell translation as a whole implies [21], [24] that, with respect to a suitable basis, $\boldsymbol{A}(\boldsymbol{k})$ has the following structure

$$
\boldsymbol{A}(\boldsymbol{k}) = \begin{pmatrix} \boldsymbol{A}_{aa}(\boldsymbol{k}) & \boldsymbol{A}_{ao}(\boldsymbol{k}) \\ \boldsymbol{A}^{\star}_{ao}(\boldsymbol{k}) & \boldsymbol{A}_{oo}(\boldsymbol{k}) \end{pmatrix} = \begin{pmatrix} O(|\boldsymbol{k}|^2) & O(|\boldsymbol{k}|) \\ O(|\boldsymbol{k}|) & O(1) \end{pmatrix} \tag{30}
$$

A straightforward computation shows that, this is obtained using the *collective cell variables*

$$
\boldsymbol{U}_a = (\boldsymbol{V} + \boldsymbol{U})/\sqrt{2}, \qquad \boldsymbol{U}_o = (\boldsymbol{V} - \boldsymbol{U})/\sqrt{2}. \tag{31}
$$

Then, a result of [21] shows that the elasticity tensor $\hat{\mathbb{C}}$ defined as

$$
\hat{\mathbb{C}}[\boldsymbol{v}\otimes\boldsymbol{k}_1]\boldsymbol{k}_2 = \left[\frac{1}{2} D^2 \boldsymbol{A}_{aa}(\boldsymbol{0})[\boldsymbol{k}_1,\boldsymbol{k}_2] - (D\boldsymbol{A}_{ao}(\boldsymbol{0})[\boldsymbol{k}_1])\, \boldsymbol{A}_{oo}^{-1}(\boldsymbol{0})\, (D\boldsymbol{A}^{\star}_{ao}(\boldsymbol{0})[\boldsymbol{k}_2])\right] \boldsymbol{v} \tag{32}
$$

defines the macroscopic elasticity of the lattice in the long wave-length approximation. This result shows also that in order to obtain the macroscopic approximation it is sufficient to obtain $\boldsymbol{A}(\boldsymbol{k})$ (mod $|\boldsymbol{k}|^2$). However exact dispersion relation are needed in order to plot the dispersion curves in the whole first Brillouin zone and to compare them to experimental data.

We postpone to the appendix the details of the computation (mod $|\boldsymbol{k}|^2$) of the dispersion matrix but note here that the final result obtained using (32) is

$$\hat{C}_{11} = a^2 \frac{A+4B}{24}, \qquad \hat{C}_{44} = a^2 \frac{2AB}{3(A+4B)}, \qquad \hat{C}_{12} = a^2 \frac{A-4B}{24}. \tag{33}$$

As the volume of the unit cell is $a^3/4$ and the total mass in the cell $2m_a$, we recover the result of subsection 2.3. Thus, the first-order approximation of the discrete model leads to the macroscopic equations of the elastodynamics with elasticities given by $C_{ij} = \hat{C}_{ij} \frac{2}{V(cell)}$ which gives, as expected, the result in (17). Once again, the cubic symmetry of the macroscopic elasticity is inherited from the microscopic symmetry of the lattice. Moreover, using a result of [22] (since we fit assumption A in Sect. 2 of [22]) the resulting macroscopic law satisfies the generalized Legendre-Hadamard condition.

Figures 1 and 2 show the experimental dispersion relations along high symmetry lines in the first Brillouin zone for silicon. Experimental data obtained by Doling [26] are illustrated in Figure 1 and the predicted dispersion relations obtained using the exact dispersion relation (28). We notice a remarkably good prediction of the dispersion data excepting the high value of the transverse acoustic branch near the X (or R) point. We also note the flatness of the dispersion data near the Γ point that we interpret this as an indication of very low numerical values of higher-order corrections based on successive approximations near the $\boldsymbol{k} = \boldsymbol{0}$.

3.3. Higher-order polynomial approximation

Computation of higher-order polynomial approximations of the acoustic branches near the center of the first Brillouin zone needs a different approach. The main

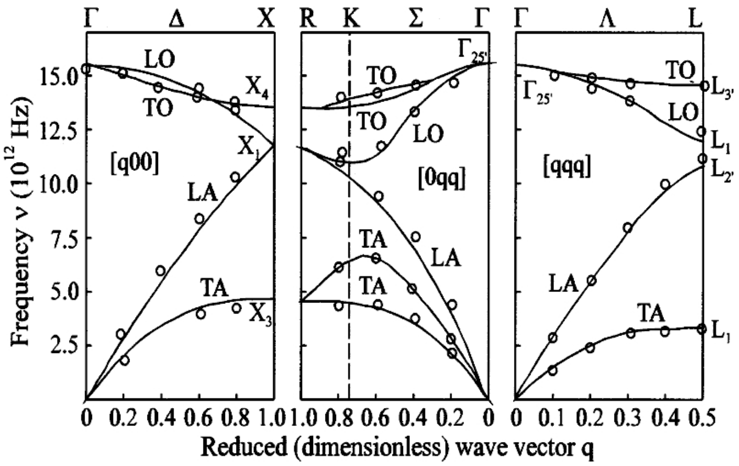

Figure 2: Experimental dispersion curves for crystalline silicon from [26], [16].

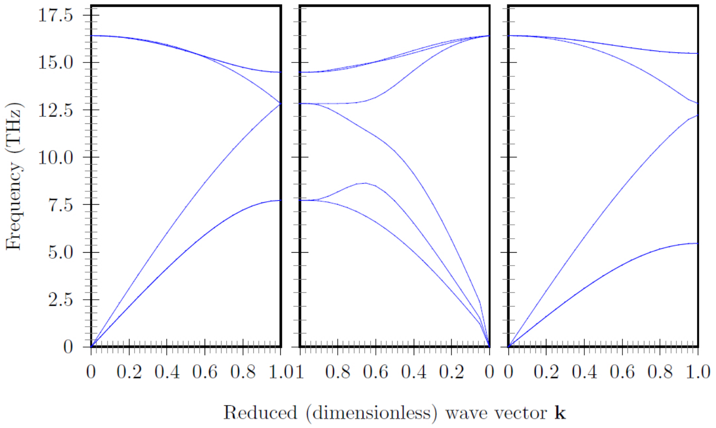

Figure 3: Computed dispersion curves for crystalline silicon using the quadratic approximation of the Keating model.

reason is that higher-order approximations of the dispersion matrix affects the splitting between the acoustic and optical branches. Two solutions of this problem exist in the literature: the first one is presented in [24] and the second one in [12]. We follow the method in [12] (also used recently in [1]) and we shall compute the third-order and the fourth-order approximations of the dispersion relations near the Γ point. In particular, we shall recover, as expected, the well-known fact that for centro-symmetric crystals the coupling constants between the deformation and it's spatial derivatives vanish[2].

The starting point of the method is the splitting of the exact dispersion matrix $\boldsymbol{A}(\boldsymbol{k})$ in (30) as

$$\boldsymbol{A}(\boldsymbol{k}) = \boldsymbol{H} + \boldsymbol{Y}(\boldsymbol{k}) + \boldsymbol{X}(\boldsymbol{k}), \tag{34}$$

where

$$\boldsymbol{H} = \begin{pmatrix} E_a \boldsymbol{I}_{3\times 3} & \boldsymbol{0}_{3\times 3} \\ \boldsymbol{0}_{3\times 3} & E_o \boldsymbol{I}_{3\times 3} \end{pmatrix}, \tag{35}$$

$$\boldsymbol{Y}(\boldsymbol{k}) = \begin{pmatrix} \boldsymbol{A}_{aa}(\boldsymbol{k}) - E_a \boldsymbol{I}_{3\times 3} & \boldsymbol{0}_{3\times 3} \\ \boldsymbol{0}_{3\times 3} & \boldsymbol{A}_{oo}(\boldsymbol{k}) - E_o \boldsymbol{I}_{3\times 3} \end{pmatrix}, \tag{36}$$

and

$$\boldsymbol{X}(\boldsymbol{k}) = \begin{pmatrix} \boldsymbol{0}_{3\times 3} & \boldsymbol{A}_{ao}(\boldsymbol{k}) \\ \boldsymbol{A}^{\star}_{ao}(\boldsymbol{k}) & \boldsymbol{0}_{3\times 3} \end{pmatrix} \tag{37}$$

and consider $\boldsymbol{X}(\boldsymbol{k})$ as the small parameter. The result in [12] can be stated as follows: splitting between the acoustic and optical branches of polynomial approximations of degree $m \leq 4$ of the exact dispersion matrix are obtained as sums $\sum_{s=0}^{m} \boldsymbol{K}^{(s)}$ where

$$\begin{aligned} \boldsymbol{K}^{(0)} &= \boldsymbol{H}, \\ \boldsymbol{K}^{(1)} &= \boldsymbol{Y}, \\ \boldsymbol{K}^{(2)} &= \frac{1}{2}[\boldsymbol{X}^H, X], \\ \boldsymbol{K}^{(3)} &= \frac{1}{2}[\boldsymbol{X}, [\boldsymbol{Y}, \boldsymbol{X}^H]^H], \\ \boldsymbol{K}^{(4)} &= \frac{1}{2}[\boldsymbol{X}, \left\{[[\boldsymbol{Y}, \boldsymbol{X}^H]^H, \boldsymbol{Y}]^H + \frac{2}{3}[\boldsymbol{K}^{(2)}, \boldsymbol{X}^H]^H\right\}] - \frac{1}{12}[[\boldsymbol{K}^{(2)}, \boldsymbol{X}^H], \boldsymbol{X}^H], \end{aligned} \tag{38}$$

the commutator $[\boldsymbol{X}, \boldsymbol{Y}]$ denotes $\boldsymbol{X}\boldsymbol{Y} - \boldsymbol{Y}\boldsymbol{X}$ and $\boldsymbol{X}^H$ is the (unique) solution $\boldsymbol{A}$ of the equation $[\boldsymbol{H}, \boldsymbol{A}] = \boldsymbol{X}$.

---

[2] This is not the case for non centro-symmetric crystals such that InP, AsP, GaAs, etc.

We notice that along the line presented above computations $mod(|\boldsymbol{k}|^m)$ still hold in order to obtain $\boldsymbol{K}^{(m)}$. A result of the previous section shows that

$$\boldsymbol{H} = \frac{8}{3}(A+4B)\begin{pmatrix} \mathbf{0}_{3\times 3} & \mathbf{0}_{3\times 3} \\ \mathbf{0}_{3\times 3} & \boldsymbol{I}_{3\times 3} \end{pmatrix}, \tag{39}$$

or, otherwise stated $E_a = 0$ and $E_o = \frac{8}{3}(A+4B)$. We obtain successively :

- For $m = 2$

$$\sum_{s=0}^{2} \boldsymbol{K}^{(s)} = \begin{pmatrix} \boldsymbol{D}_{aa}^{(2)} & \mathbf{0}_{3\times 3} \\ \mathbf{0}_{3\times 3} & \ldots \end{pmatrix} \tag{40}$$

  where

$$\boldsymbol{D}_{aa}^{(2)} = \frac{a^2}{24(A+4B)}\begin{pmatrix} f^{(2)}(k_1,k_2,k_3) & g^{(2)}(k_1,k_2,k_3) & g^{(2)}(k_1,k_3,k_2) \\ g^{(2)}(k_2,k_1,k_3) & f^{(2)}(k_2,k_3,k_1) & g^{(2)}(k_2,k_3,k_1) \\ g^{(2)}(k_3,k_1,k_2) & g^{(2)}(k_3,k_2,k_1) & f^{(2)}(k_3,k_1,k_2) \end{pmatrix} \tag{41}$$

  and

$$\begin{aligned} f^{(2)}(k_1,k_2,k_3) &= (A^2+48B^2)k_1^2 + 16AB|\boldsymbol{k}|^2, \\ g^{(2)}(k_1,k_2,k_3) &= (A^2+16AB-16B^2)k_1k_2. \end{aligned}$$

  Since the unit cell has volume $a^3/4$ and two atoms we identify

$$\frac{a^2}{24(A+4B)}(A^2+48B^2)k_1^2 + 16AB|\boldsymbol{k}|^2 = \frac{a^3}{8}\left[C_{11}k_1^2 + C_{44}(k_2^2+k_3^2)\right]$$

  and

$$\frac{a^2}{24(A+4B)}(A^2+16AB-16B^2)k_1k_2 = \frac{a^3}{8}C_{12}k_1k_2.$$

  This identification gives, as expected, the elastic constants of the previous section, i.e.

$$C_{11} = \frac{A+12B}{3a}, \qquad C_{12} = \frac{A-4B}{3a}, \qquad C_{44} = \frac{16AB}{3a(A+4B)}.$$

- For $m = 3$

$$\boldsymbol{K}^{(3)} = \mathbf{0} \quad \Rightarrow \quad \sum_{s=0}^{3} \boldsymbol{K}^{(s)} = \sum_{s=0}^{2} \boldsymbol{K}^{(s)}. \tag{42}$$

- For $m = 4$

$$\sum_{s=0}^{4} \boldsymbol{K}^{(s)} = \begin{pmatrix} \boldsymbol{D}_{aa}^{(2)} + \boldsymbol{D}_{aa}^{(4)} & \mathbf{0}_{3\times 3} \\ \mathbf{0}_{3\times 3} & \cdots \end{pmatrix} \tag{43}$$

where $\boldsymbol{D}_{aa}^{(4)}$ is the fourth-order homogeneous polynomial with the same structure as $\boldsymbol{D}_{aa}^{(2)}$ but now

$$f^{(4)}(k_1, k_2, k_3) = \hat{f}_{122122}(k_2^4 + k_3^4) + 6\hat{f}_{122133} k_2^2 k_3^2 + 6\hat{f}_{211222} k_1^2 (k_2^2 + k_3^2)$$

and

$$g^{(4)}(k_1, k_2, k_3) = (4\hat{f}_{112222}(k_1^2 + k_2^2) + 12\hat{f}_{112233} k_3^2) k_1 k_2.$$

A long but straightforward computation of coefficients in $f^{(4)}$ and $g^{(4)}$ provides :

$$\begin{aligned} \hat{f}_{122122} &= -a^4 \frac{(A-4B)^2(7A^2 + 40AB + 112B^2)}{4608(A+4B)^3}, \\ \hat{f}_{122133} &= -a^4 \frac{(A-4B)^3(13A + 44B)}{13824(A+4B)^3}, \\ \hat{f}_{211222} &= -a^4 \frac{(A-4B)^2(13A^2 + 88AB + 208B^2)}{27648(A+4B)^3}, \\ \hat{f}_{122222} &= -a^4 \frac{(A-4B)^2(5A^2 + 32AB + 80B^2)}{(A+4B)^3}, \\ \hat{f}_{112233} &= \hat{f}_{122133}. \end{aligned} \tag{44}$$

Remarks :

(i) We notice that $\boldsymbol{K}^{(3)} = \mathbf{0}$ means that there is no coupling between the first derivatives of the strain and the strain itself in the free-energy density of the continuum approximation. This result can be obtained directly from group representation theory using the symmetry properties of the centre-symmetric lattice.

(ii) As in the second-order approximation, we can define $f = \frac{2}{V(cell)}\hat{f}$. The two qualitative results: $f_{111111} = 0$ and $f_{112233} = f_{122133}$ are specific to the the discrete VFF model.

(iii) The dynamics of the continuum model obtained above is governed by

$$\rho\ddot{\boldsymbol{u}}_i = C_{ijkl}u_{k,lj} + f_{ijklmn}u_{k,lmnj}. \tag{45}$$

It follows that the ratio between f_{ijklmn} and C_{ijkl} provides one (or several) estimates for the characteristic lengths of the approximate model. In our case $f \simeq 10^{-10}N$ and $C \simeq 10^{10}N/m^2$ which predicts internal length scale of $\simeq 1$ Angstrom.

(iv) The material parameters of the second-gradient approximation of the discrete model can be computed numerically using the values of A and B from the discrete VFF model. Using (44) and (17) we obtain

$$f_{122122} = -3.37 \times 10^{-10}\ \text{N}, \quad f_{122133} = -1.24 \times 10^{-10}\ \text{N},$$

$$f_{112222} = -1.24 \times 10^{-10}\ \text{N}, \quad f_{112233} = -1.24 \times 10^{-10}\ \text{N},$$

$$f_{211222} = -1.10 \times 10^{-10}\ \text{N}.$$

We notice here that they are one order of magnitude lower than those obtained using *ab initio* and molecular dynamics simulations in [1]. This result enforce the conclusion that *the internal length introduced in the continuum model using approximation of the dispersion relation near the* Γ *point is insignificant* unless the specimen size is un-physically small. As already noted, we interpret this result as a consequence of the fact that near the Γ point the dispersion relations are *almost* linear expressions (see figure 2). It follows that corrections near the center of the first Brillouin zone will not improve significantly the previously obtained approximations of the dispersion curves. A different alternative is proposed in [25] where, in the one dimensional case, approximative models based on a qualitative different method (such as Padé interpolation, or approximation of first roots) were studied.

(v) The above computation gives the coefficients of the dynamic equation of motion which is a continuum approximation of the discrete model. It should be also noticed that, as shown in [1], [4] and [5], in the multidimensional case, the coefficients in the equation of the motion *do not determine in an unique manner the analytical expression of the free-energy.* Thus, as already discussed in [1], the sign paradox in the multidimensional can be avoided.

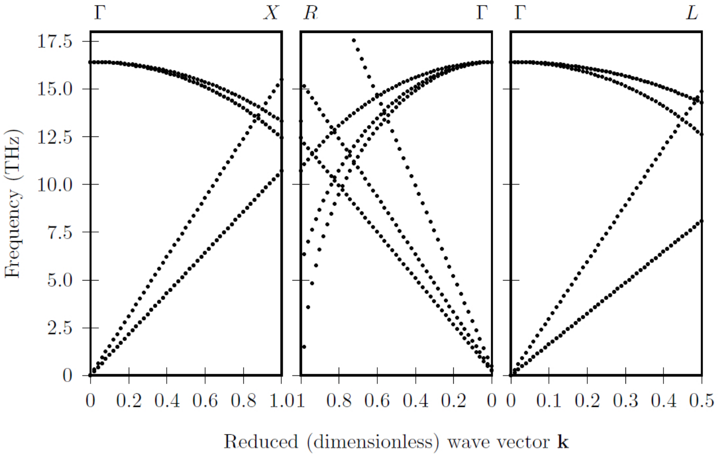

Figure 4: Computed dispersion curves for crystalline silicon using the second-order polynomial approximation. For comparaison with the experimental data we have plotted the dispersion curves only in the first Brillouin zone along the high symmetry lines; in this approximation acoustic branches are straight lines with slopes depending on the elastic constants. In this approximation $\omega_a(\boldsymbol{k})$ is always real.

In figures 4 and 5 we have represented the theoretical dispersion relations (real part of acoustic and optical branches) along the high symmetry lines in the first Brillouin zone. Topological characteristics (multiplicity, etc.) are conserved and, as expected, the first-order approximation leads to linear dispersion relations for the acoustic branches. The second order-approximation illustrates a well-known behavior of the acoustic branch (also discussed in [6], [27]): it

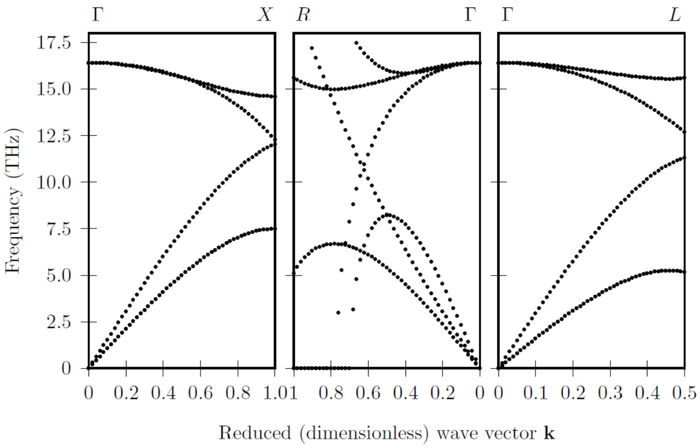

Figure 5: Computed dispersion curves for crystalline silicon using the fourth-order polynomial approximation. We have represent only the real part of the acoustic branches on high symmetry lines. As noted in the last paragraph of section 3, the imaginary part of $\omega(\boldsymbol{k})$ does not vanish.

cross the horizontal axis at finite values of wavelength. This is related to the instability of the elastic response for continuum models which represent approximations of discrete systems. A different discrete-to-continuum method able to correct this unphysical behavior was proposed in [28].

4. A model with hyper-pre-stress

An alternative to the higher order continuum theory, which also introduces an internal length in the discrete model was presented in [2] in the one dimensional setting. The key ingredient is the competition between two force systems with different reference lengths. The analysis of the simplest one-dimensional model with near-neighbors (NN) and next-to-near neighbors (NNN) interactions with *incompatible references lengths* evidence surface energy associated with free-boundaries and a size-effect. In this section we shall adopt the ideas in [2] and modify the discrete VFF model in order to predict both (a) the bulk elasticity of cristalline diamond-like structures and (b) surface effects associated to *relaxation* near free-boundaries. The constructed model incorporates an internal length that can be calibrated so as to fit the observed lattice parameter evolution determined experimentally .

The starting point is the quadratic approximation of the Keating model including two equilibrium lengths, further denoted l_1 and l_2 and associated to central and non-central interaction energies. Thus, the total elastic energy of the model becomes

$$W = \sum_{(i,j)} \frac{A}{2} \left[(\vec{u}^j - \vec{u}^i) \cdot \vec{n}^{ij} - l_1 \right]^2 + \sum_{(i,j,k)} \frac{B}{2} \left[(\vec{u}^j - \vec{u}^i) \cdot \vec{n}^{ki} + (\vec{u}^k - \vec{u}^i) \cdot \vec{n}^{ji} - l_2 \right]^2 . \tag{46}$$

4.1. Infinite lattice : macroscopic behavior and incompatibility

Using (46) and the method in subsection 2.3 we obtain, in an infinite crystal, the macroscopic constitutive relation in the form

$$\boldsymbol{\sigma} = \mathbb{C}[\boldsymbol{\varepsilon} - \boldsymbol{\varepsilon}_0] \tag{47}$$

where $\boldsymbol{\varepsilon}_0 = \varepsilon_0 \boldsymbol{I}$,

$$\varepsilon_0 = \frac{4\sqrt{3}}{a} \frac{Al_1 - 2Bl_2}{3A + 4B}.$$

With respect to the reference configuration used to write (46), the macroscopic elastic constants are still given by (17). It follows that in an infinite lattice (or far from the boundary in a finite domain) the overall lattice parameter for a free bulk material is

$$\hat{a} = a(1 + \varepsilon_0) = a \left(1 + \frac{4\sqrt{3}}{a} \frac{Al_1 - 2Bl_2}{3A + 4B} \right), \tag{48}$$

but the physical meaning of a is not *the ground state lattice parameter* but just *an arbitrary reference length*, with respect to which displacements in (46) are measured.

Following a parallel to the one-dimensional case presented in Charlotte and Truskinovsky [2], in (46) we have to distinguish between the two cases of *compatible* and *incompatible* reference lengths.

In the following, two reference lengths l_1 and l_2 will be called *compatible* if and only if

$$2l_1 + 3l_2 = 0. \tag{49}$$

Otherwise, the couple (l_1, l_2) will be called *incompatible*.

The result in (48) shows that when the reference configuration is submitted to a macroscopic deformation $\varepsilon_0 \boldsymbol{I}$ (pure dilation or compression, depending on the sign of $Al_1 - 2Bl_2$) the lattice parameter changes from a to $\hat{a}$ and the lattice reach it's ground state. With respect to this new (reference) configuration the elastic energy is

$$W = \sum_{(i,j)} \frac{A}{2} \left[(\vec{u}^j - \vec{u}^i) \cdot \vec{n}^{ij} - L_1 \right]^2 + \sum_{(i,j,k)} \frac{B}{2} \left[(\vec{u}^j - \vec{u}^i) \cdot \vec{n}^{ki} + (\vec{u}^k - \vec{u}^i) \cdot \vec{n}^{ji} - L_2 \right]^2 \tag{50}$$

where

$$L_1 = l_1 - \frac{\sqrt{3}}{4} \varepsilon_0 a, \qquad L_2 = l_2 + \frac{1}{2\sqrt{3}} \varepsilon_0 a. \tag{51}$$

Note that the couple (L_1, L_2) is the unique couple with the properties

$$2L_1 + 3L_2 = 2l_1 + 3l_2, \qquad AL_1 - 2BL_2 = 0. \tag{52}$$

The first equation in (52) shows that the *incompatibility is conserved* by changes in the reference configuration, while the second one reflects the fact that at lattice parameter $\hat{a}$ we are in the ground state. Without loosing the generality, we shall use in the following (50) so that the bulk material behavior is described by

$$C_{11} = \frac{A + 12B}{3\hat{a}}, \qquad C_{12} = \frac{A - 4B}{3\hat{a}}, \qquad C_{44} = \frac{16AB}{3\hat{a}(A + 4B)} \tag{53}$$

and the elastic energy density is, up to an additive constant, $W = \frac{1}{2}\mathbb{C}[\boldsymbol{\varepsilon}] : \boldsymbol{\varepsilon}$.

4.2. Hyper-pre-stress in the finite lattice

As noted in [2] including incompatible references in the lattice is equivalent to *a self-equilibrated force system* acting on each particle. The following remarks provide more insight on the rôle of the reference lengths:

1. Assume (L_1, L_2) *compatible* and consider a finite free-lattice. Then the minimum of the total elastic energy (46) is attained (up to a rigid body displacement) by the homogeneous displacement given by

   $$\boldsymbol{u}^i = \boldsymbol{E}_0\boldsymbol{x}^i \qquad \text{for} \qquad \boldsymbol{E}_0 = \varepsilon_0\boldsymbol{I} \qquad \text{and} \qquad \varepsilon_0 = 4L_1/(\sqrt{3}a). \tag{54}$$

   This result can be easily verified since in the case of compatible reference lengths the minimum of the total elastic energy is zero.

2. In the following, a particle of a finite-lattice will be called *completely coordinated* if all it's NN and NNN neighbors belong to the structure. Otherwise, the particle is called *incompletely coordinated.* Then, *in the reference configuration, for a fully coordinated particle the force system acting on it is self-equilibrated.* In order to prove this assertion we shall denote by i a fixed particle and by j_α $(\alpha = 1, 2, 3, 4)$ it's four near-neighbors. Taking into account the expressions of the central and non-central forces acting on particle i we obtain:

   - The sum of central forces

     $$\left[-A\sum_{j\in NN(i)}[(\boldsymbol{u}^j - \boldsymbol{u}^i)\cdot\boldsymbol{n}^{ij} - L_1]\boldsymbol{n}^{ij}\right]_{\boldsymbol{u}^i=\boldsymbol{u}^j=\boldsymbol{0}} = AL_1\sum_{j\in NN(i)}\boldsymbol{n}^{ij} = \boldsymbol{0}. \tag{55}$$

     due to the geometry of the diamond structure.

   - The sum of non-central forces is

     $$\left[\sum_{\substack{j,k\in NN(i)\\ j\neq k}}\frac{\partial w_i^{jk}}{\partial \boldsymbol{u}^i} + \sum_{j\in NN(i)}\left(\sum_{\substack{k\in NN(j)\\ k\neq i}}\frac{\partial w_j^{ik}}{\partial \boldsymbol{u}^i}\right)\right]_{\boldsymbol{u}^i=\boldsymbol{u}^j=\boldsymbol{u}^k=\boldsymbol{0}} \tag{56}$$

The explicit computation of the first sum in (56) gives

$$BL_2 \sum_{\substack{j,k \in NN(i) \\ k \neq j}} (\boldsymbol{n}^{ij} + \boldsymbol{n}^{ik}) = 3BL_2 \sum_{j \in NN(i)} \boldsymbol{n}^{ij}, \tag{57}$$

and vanish due to the symmetry of the diamond lattice (as in (55)), while the second sum is

$$-BL_2 \sum_{j \in NN(i)} \sum_{\substack{k \in NN(j) \\ k \neq i}} \boldsymbol{n}^{jk} = -3BL_2 \sum_{j \in NN(i)} \boldsymbol{n}^{ij} = \boldsymbol{0}. \tag{58}$$

after rearrangement. It is interesting to notice here that the right-hand sides of (57) and (58) show that the sum in (56) vanish even without the symmetry of the diamond structure.

3. A different perspective the second remark is obtained noting that for a free finite-lattice (and up to a rigid displacement of the lattice) the displacement that realizes the minimum of the total energy given in (46) realizes also the minimum of

$$\sum_{(i,j)} w_i^j + \sum_{(i,j,k)} w_i^{jk} - \sum_{i \in IC} \boldsymbol{f}^i \cdot \boldsymbol{u}^i \tag{59}$$

where the first two sums represent the total elastic energy in the original VFF model (5) and the third one may be regarded as the work of external forces $\boldsymbol{f}^i$ acting only on *incompletely coordinated* particles. To prove this we note that the development of (5) provide three terms: a quadratic part with respect to the displacement, denoted W_2, which is exactly (5), a constant term, denoted W_0, that do not affect the minimum and a term homogeneous of degree one with respect to the displacement, denoted W_1. Our previous remark shows that in the general expression

$$W_1 = \sum_i \boldsymbol{f}^i \cdot \boldsymbol{u}^i \tag{60}$$

the factors of $\boldsymbol{u}^i$ vanish for completely coordinated particles, which proves the assertion.

Assertions (1) and (2) show that when the reference lengths are incompatible the self-equilibrated force system introduced by the hyper pre-stress produces a boundary layer effect in the finite lattice.

Using (52.2) with respect to the ground state of an infinite lattice, the elastic energy is :

$$W = \sum_{(i,j)} \frac{A}{2} \left[(\vec{u}^j - \vec{u}^i) \cdot \vec{n}^{ij} - L_1 \right]^2 +$$

$$+ \sum_{(i,j,k)} \frac{B}{2} \left[(\vec{u}^j - \vec{u}^i) \cdot \vec{n}^{ki} + (\vec{u}^k - \vec{u}^i) \cdot \vec{n}^{ji} - L_1 \frac{A}{2B} \right]^2 . \qquad (61)$$

The above model has the following properties :

- The lattice parameter in an infinite lattice is $\hat{a}$.
- The elastic constants obtained using (53) fit the experimental data; dispersion curves are those presented in figures (3).
- The model includes an adjustable internal length so that, in a finite domain, it has a *size-dependent lattice parameter*.

A straightforward consequence of the last property is that the model will also predict a size-dependent Young modulus. Due to analytical complexity of the multidimensional case we are not able to present a complete analysis following the line in [2] but instead we shall illustrate the main features of the obtain model using numerical simulations.

We note that a positive (negative) sign of L_1 induces in a finite domain an average lattice parameter larger (smaller) than that of an infinite lattice. As these effects are similar we shall focus the numerical study of the case $L_1 > 0$ (average lattice parameter of finite structure larger that of the infinite lattice) as indicates experimental data obtained using Raman spectroscopy for porous silicon. The reverse phenomena can be obtained (average lattice parameter of finite structures lower than that of an infinite lattice) by changing the sign of L_1.

5. Size effects in finite structures

5.1. *Average lattice parameter for finite structures*

In order to illustrate the size-effect induced by the hyper-pre-stress we have performed numerical computations of the average lattice parameter for silicon free-structures with different characteristic lengths. For simplicity, we have considered only parallelipipedic structures oriented along the crystallographic axes.

We choose for the material parameters A and B the values given in Table (2.3), $\hat{a}$ used as the reference configuration equals 5.431 Åand L_1 was fixed to 1% of the interatomic distance of the infinite lattice, i.e. $\sqrt{3}/4\hat{a}$. We choose $L_2 = \frac{A}{2B} L_1$ in order to measure the deviation of the average lattice parameter from the ideal infinite lattice, so the reference configuration it that of the ground state of the infinite lattice.

We have considered nano-structures with lateral dimensions (α, l, l) - also called in the following *plate-like* structures, (α, α, l) - also called *beam-like* structures, and (α, α, α) - also called *bulk-like* structures, for $l = 10$ nm (which corresponds to 20 mono-layers) and α between 2 nm and 10 nm. Figure 6 shows the obtained numerical results for the deviation of the average lattice parameter with respect to that of the infinite lattice. As expected, for $L_1 > 0$ (respectively ¡0) the average lattice parameter increases (decreases) when one characteristic dimension of the structure decreases, but tends to $\hat{a}$ (which is the average lattice parameter of an infinite lattice) when all dimensions of the structure are very large. At this limit the continuum theory applies and surface effects can be neglected. Figure 6 also indicates, as expected, that for fixed l, for bulk-like structures the average lattice parameter increases faster than for beam-like structures, and for beam-like structures the lattice parameter increases faster than for plate-like structures when α varies. This is obviously the effect of the specific surface available for different shapes.

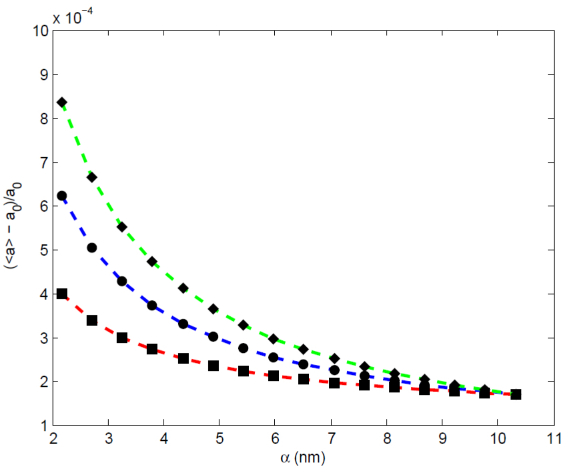

Figure 6: The average lattice parameter for finite plate-like structures with lateral dimensions (α, l, l) (■), beam-like structures with lateral dimensions (α, α, l) (●) and bulk-like structures with lateral dimensions (α, α, α) (◆) for 2 nm $< \alpha <$ 10nm, and $l = 10$ nm.

5.2. Porosity dependent lattice parameter in porous silicon

Porous silicon is a nano-structured material obtained using electrochemical anodization in a solution of fluorhydric acid (HF) and ethanol [29]. Depending on the size of the pores [30], one can speak about nanoporous silicon when the size of crystallites is less than 5 nm, about mesoporous silicon when the pore sizes range between 5 nm and 50 nm and macroporous silicon when the pores sizes are larger than 50 nm. From an experimental point of view, the porosity is controlled by the anodization current density, anodization time and HF/ethanol ratio. The obtained pores are inter-connected as they have been obtained by the action of the HF/ethanol solution on bulk Si.

In the case of nanoporous silicon the specific area can reach very large values as for exemple 100 m^2/g. In such situations one can expect that the mechanical behavior of the material is largely dominated by the ”surface effects”. It follows that the porous silicon is a particularly interesting object in order to understand deviations from classical bulk properties and size effects in elastic (covalent)

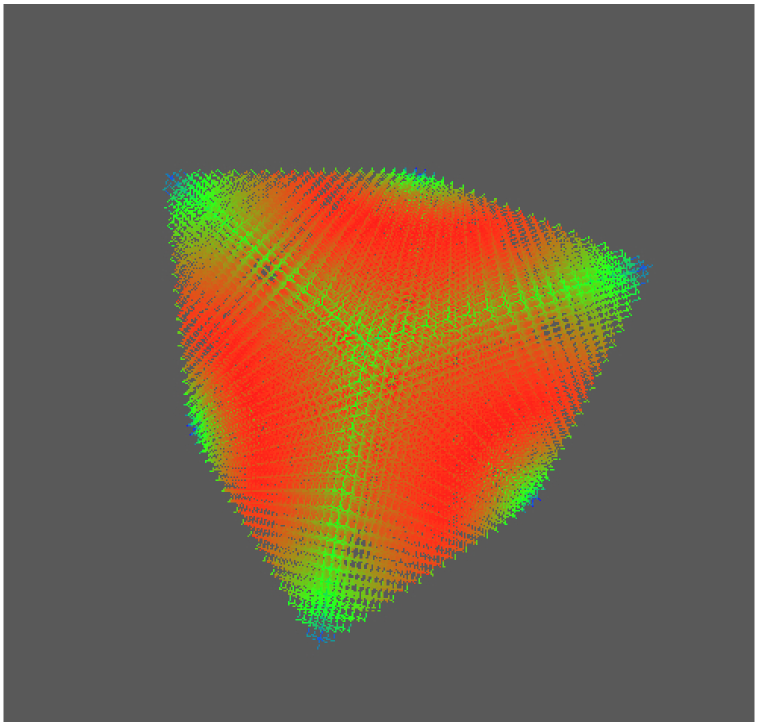

Figure 7: Stress-free configuration illustrating relaxation near the boundary, edges and vertexes on a 10 nm^3 bulk silicon block using the model with hyper-pre-stress.

crystals.

Generally, real three-dimensional crystal surfaces present an additional difficulty due to the recombination (of electrostatic nature) of surface bonds. Thus, surface reconstruction always induces additional deformation near the free-surfaces so that, generally, both the size-effect mentioned above and the surface reconstruction together contribute to the elasticity of nano-scale objects. In very special circumstances one can distinguish between these two sources of deformation near free-surfaces of crystals. Electrochemical anodization used to obtain porous silicon avoids surface recombination since the chemical reactions implied in the process result in Si-H terminated surface.

During anodization the lattice parameter is measured using X-ray diffraction

(XRD) and/or Raman spectroscopy. When anodization is performed on a part of a bulk specimen the porous silicon conserves the crystallographic directions of the original bulk specimen but

- the lattice parameter in the [001] direction is larger than the bulk lattice parameter,
- the lattice parameter in the [100] and [010] directions are the same as in the bulk.

This behavior is commonly presented as a *relaxation* of porous silicon due to porosification, and is interpreted as the manifestation of a modification of the average lattice parameter under the constraint of ”no lateral motion”. Experimental data concerning the modification of the (average) lattice parameter induced by anodization as a function of porosity was measured in ([31], [32]) and is plotted in figure 8.

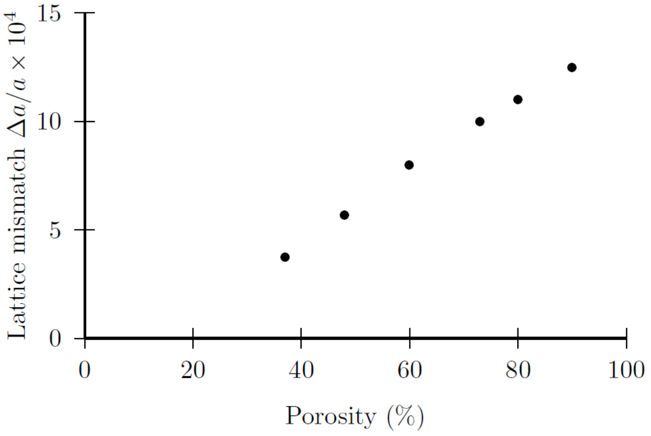

Figure 8: Lattice mismatch as a function of porosity after anodization (experimental data from [31]).

In order to explore the porosity-dependent lattice parameter predicted by our model we have considered a cubic super-cell oriented along the crystallographic axes and containing a one-parameter connected pore. The volume of the porous super-cell is obtained eliminating the atoms inside the union of the three cylinders $\mathcal{C}_i = \{(x_1, x_2, x_3), max(|x_j|, |x_k|) \leq \alpha\}$ for $i = 1, 2, 3$. A typical super-cell obtained with this method is illustrated in figure 10.

The computational procedure involves the following steps :

1. At fixed super-cell size and porosity (α fixed) we solve the discrete homogenization problem with periodic boundary conditions and deduce the macroscopic relation in the form
$$\boldsymbol{\Sigma} = \mathbb{C}(\alpha)[\boldsymbol{E} - \boldsymbol{E}_0(\alpha)].$$
At this point both the macroscopic elasticity and the pre-strain are porosity dependent. As expected, using (61) we obtain $\boldsymbol{E}_0(0) = \mathbf{0}$ (as the bulk material is self-equilibrated) and $\mathbb{C}(0)$ is given by (53). The computation of macroscopic coefficients for the bulk material (vanishing porosity) is independent on the cell-size.
2. Since the porous material in constraint in the lateral directions but free in the vertical one we conclude that the vertical strain induced by the pre-strain, porosity and lateral constraint is given by
$$E_{33} = (1 + 2\frac{C_{12}}{C_{11}}\boldsymbol{E}_0. \tag{62}$$

We fit the new material parameter L_1 so as to obtain one of the experimental data - the deformation at 50% porosity. The value of L_1 obtained using only this data was used to predict the average lattice parameter at different porosities. The obtained numerical results are illustrated on figure **??**. We note :

- a linear regime at small porosities in agreement with experimental data;
- an increasing average lattice-parameter at larger porosities in disagreement with experimental data.

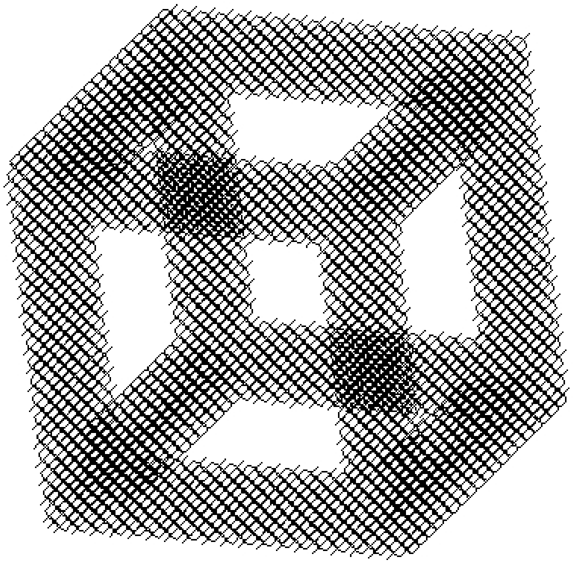

Figure 9: Typical geometry of a super-cell (containing here 20.000 atoms) used to compute the average lattice-parameter for porous Si using the model with hyper-pre-stress.

We notice that interpretation of Raman spectroscopy data (one of the method used in experiments) needs macroscopic behavior law of the porous material - partially available in the literature [33]. In this context, the Vegard law overestimates the macroscopic elasticities which in turn leads to a underestimate of the lattice parameter in high range porosity. We notice also that the particular geometry we have used induces a macroscopic law with cubic symmetry. This is not the case if one consider only a vertical pore in the super-cell in which case the macroscopic law will posses transversal isotropy. The actual method answer also the question of a porosity dependent lattice parameter for nano-porous

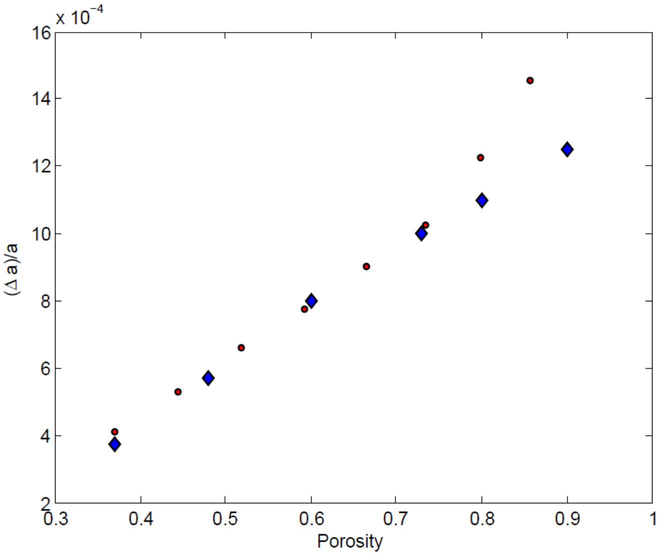

Figure 10: Numerical results for the porosity-dependent vertical induced deformation as a function of porosity; we interpret the larger lattice-parameter predicted by the model in the high porosity range as a numerical drawback due to limited computational size.

silicon. For larger systems, as is the case of the macro-porous silicon, the modification of the average lattice parameter induces by $\boldsymbol{E}_0$ will be insignificant as bulk behavior dominates the surface effects.

6. Overview and conclusions

In this paper we have investigated two alternative solutions intended to include an internal length is the discrete model of Keating in order to fit both (a) the macroscopic elasticity of crystals with diamond-like structure and (b) a size-dependent lattice parameter (evidenced by Raman spectrosocpy).

The first solution consists in considering successive continuum approximations of the discrete model. The second-order polynomial approximation of the dispersion relation near the center of the first Brillouin zone gives the continuum elasticity theory but does not incorporate an internal length. The next approximation leads to a second-gradient model which includes several internal lengths but the model obtained have some intrinsic drawbacks. Starting with a realistic discrete elastic model that includes pair interactions and three-body interactions, we compute explicitly all fourth-order material parameters of the second-gradient theory obtained using polynomial approximation of the acoustic branches and show that, in agreement with previously obtained results [1], the internal length obtained are too small to apply to realistic situations. This conclusion can be anticipated from the dispersion relations which show almost linear dependence on the wave number near the Γ point.

The second solution we present includes incompatible reference lengths in the valence force field model. This is equivalent to a self-equilibrated force system acting on each atom in the reference configuration. In agreement with results obtained in the one-dimensional case [2] we show that average lattice parameter of finite structures deviates from the ideal lattice parameter of an infinite lattice. We study numerically the size-dependent average lattice parameter for stress-free finite beam-like, plate-like and bulk-like nano-structures and evidence not only a size effect but also a shape effect. In the particular case of nano-porous silicon, we can fit the material parameters of the model with hyper-pre-stress so as to fit experimental results obtained in [31]) in the range of moderate porosities. At very large porosities ($> 80\%$), due to limited size of our computation, the size-effect of small cross-section beam-like crystallites dominates the numerical results so that the predicted values diverge from the measured data. The application of the model with hyper-pre-stress for the prediction of hardening/softening in nano-structures will be discussed in a future work.

Acknowledgement

We gratefully acknowledge helpful discussions and comments with G. Grenet and partial financial support by the National Research Agency (ANR) through the projetc SPAME – 06-0274.

References

[1] R. Maranganti, P. Sharma, A novel atomistic approach to determine strain-gradient elasticity constants: Tabulation and comparison for various metals, semiconductors, silica, polymers and the (ir) relevance for nanotechnologies, Journal of the Mechanics and Physics of Solids 55 (9) (2007) 1823 – 1852.

[2] M. Charlotte, L. Truskinovsky, Linear elastic chain with a hyper-pre-stress, Journal of the Mechanics and Physics of Solids 50 (2) (2002) 217 – 251.

[3] H. E. H.S. Park, W. Cai, H. Huang, Mechanics of crystalline nanowires, MRS Bulletin 34 (2009) 178 – 183.

[4] R. Mindlin, Second gradient of strain and surface tension in linear elasticity, Int. J. Solids and Structures 1 (1965) 417–438.

[5] R. Mindlin, Microsctructure in linear elasticity, Archive for Rat. Mech. and Analysis 16 (1964) 51–78.

[6] A. Metrikine, H. Askes, One-dimensional dynamically consistent gradient elasticity models derived from a discrete microstructure: Part 1: Generic formulation, European Journal of Mechanics - A/Solids 21 (4) (2002) 555 – 572.

[7] R. Toupin, Elastic materials with couple stresses, Arch. Rational Mech. Anal. 11 (1962) 385 – 414.

[8] S. Forest, Milieux Continus Généralisés et Matériaux Hétérogénes, Vol I and II, Les presses Mines ParisTech, 2006.

[9] D. C. C. Lam, F. Yang, A. C. M. Chong, J. Wang, P. Tong, Experiments and theory in strain gradient elasticity, Journal of the Mechanics and Physics of Solids 51 (8) (2003) 1477 – 1508.

[10] N. Fleck, J. Willis, A mathematical basis for strain-gradient plasticity theory–part i: Scalar plastic multiplier, Journal of the Mechanics and Physics of Solids 57 (1) (2009) 161 – 177.

[11] N. Fleck, J. Willis, A mathematical basis for strain-gradient plasticity theory. part ii: Tensorial plastic multiplier, Journal of the Mechanics and Physics of Solids 57 (7) (2009) 1045 – 1057.

[12] D. P. DiVincenzo, Dispersive corrections to continuum elastic theory in cubic crystals, Phys. Rev. B 34 (8) (1986) 5450–5465.

[13] J. Tersoff, New empirical approach for the structure and energy of covalent systems, Phys. Rev. B 37 (12) (1988) 6991–7000.

[14] F. Herman, Lattice vibrational spectrum of germanium, Journal of Physics and Chemistry of Solids 8 (1959) 405 – 418.

[15] P. N. Keating, Effect of invariance requirements on the elastic strain energy of crystals with application to the diamond structure, Phys. Rev. 145 (2) (1966) 637–645.

[16] I. P. T. Institute, Physical properties of semiconductors, http://www.ioffe.ru/SVA/NSM/ .

[17] M. Daw, M. Baskes, Embedded-atom method: Derivation and application to impurities, surfaces, and other defects in metals, Phys. Rev. B 29 (12) (1984) 6443–6453.

[18] M. Daw, M. Baskes, Semiempirical, quantum mechanical calculation of hydrogen embrittlement in metals, Phys. Rev. Lett. 50 (17) (1983) 1285–1288.

[19] A. E. Carlsson, N. W. Ashcroft, Pair potentials from band theory: Application to vacancy-formation energies, Phys. Rev. B 27 (4) (1983) 2101–2110. doi:10.1103/PhysRevB.27.2101.

[20] A. E. Carlsson, P. A. Fedders, C. W. Myles, Generalized embedded-atom format for semiconductors, Phys. Rev. B 41 (2) (1990) 1247–1250. doi:10.1103/PhysRevB.41.1247.

[21] A. Mielke, Macroscopic behavior of microscopic oscillations in harmonic lattices via wigner-husimi transforms, Arch. Rational Mech. Anal. 181 (3) (2006) 401–448.

[22] E. Weinan, P. Ming, Cauchy-born rule and the stability of crystalline solids: Static problems, Arch. Rational Mech. Anal. 183 (2) (2007) 241–297.

[23] J. Krumhansl, Mechanics of Generalized Continua (E. Kroner ed.), Proc. IUTAM Symposium on the Generalized Cosserat Continuum Theory of Dislocations with Applications, Springer, 1967, Ch. Some considerations of the relation between solid state physics and generalized continuum mechanics, pp. 298–311.

[24] I. Kunin, Elastic Media with Microsctructure, Vol I and II, Springer, 1982 and 1983.

[25] M. Charlotte, L. Truskinovsky, Towards multi-scale continuum elasticity theory, Continuum Mechanics and Thermodynamics 20 (3) (2008) 133–161.

[26] G. Dolling, Proc. symp. inelastic scattering neutrons in solids and liquids, Chalk River 2 (1963) 37.

[27] H. Askes, A. V. Metrikine, One-dimensional dynamically consistent gradient elasticity models derived from a discrete microstructure: Part2: Static

and dynamic response, European Journal of Mechanics - A/Solids 21 (4) (2002) 573 – 588.

[28] A. V. Metrikine, H. Askes, One-dimensional dynamically consistent gradient elasticity models derived from a discrete microstructure: Part 1: Generic formulation, European Journal of Mechanics - A/Solids 21 (4) (2002) 555 – 572.

[29] O. Bisi, S. Ossicini, L. Pavesi, Porous silicon: a quantum sponge structure for silicon based optoelectronics, Surface Science Reports 38 (1-3) (2000) 1 – 126.

[30] R. Herino, W. L. (eds.), Porous silicon and related materials, Thin Solid Films 255.

[31] D. Bellet, G. Dolino, X-ray diffraction studies of porous silicon, Thin Solid Films 276 (1-2) (1996) 1 – 6, papers presented at the European Materials Research Society 1995 Spring Conference, Symposium I: Porous Silicon: Material, Technology and Devices.

[32] K. Barla, R. Herino, G. Bomchil, J. C. Pfister, A. Freund, Determination of lattice parameter and elastic properties of porous silicon by x-ray diffraction, Journal of Crystal Growth 68 (3) (1984) 727 – 732.

[33] L. C. (ed.) (Ed.), EMIS Data reviews, Vol. 17, The Institution of Engineering and Technology, 1997.

Appendix - Dispersion relation $\boldsymbol{mod(k^2)}$

We present here the details of the computation leading from (25) to (33). For convenience, we shall introduce the following notations

$$\boldsymbol{P} = \begin{pmatrix} 0 & k_1k_2 & k_1k_3 \\ k_1k_2 & 0 & k_2k_3 \\ k_1k_3 & k_2k_3 & 0 \end{pmatrix}, \quad \boldsymbol{T} = \begin{pmatrix} k_1^2 & 0 & 0 \\ 0 & k_2^2 & 0 \\ 0 & 0 & k_3^2 \end{pmatrix}, \quad \boldsymbol{S} = \begin{pmatrix} 0 & k_3 & k_2 \\ k_3 & 0 & k_1 \\ k_2 & k_1 & 0 \end{pmatrix}. \tag{63}$$

The block $\boldsymbol{A}_{UU}$ is ($mod|\boldsymbol{k}|^2$) the sum of :

$$A \sum_{j\in NN(i)} \boldsymbol{E}_i^{jj} = \frac{4A}{3}\boldsymbol{I}, \tag{64}$$

$$B \sum_{\substack{\{j,k\}\subset NN(i)\\ k\neq j}} (\boldsymbol{E}_i^{jj} + \boldsymbol{E}_i^{kj} + \boldsymbol{E}_i^{kk} + \boldsymbol{E}_i^{jk}) = \frac{8B}{3}\boldsymbol{I}, \tag{65}$$

$$B \sum_{\substack{j\in NN(i)\\ k\in NN(j)\\ k\neq i}} \boldsymbol{E}_j^{kk} = 3B \sum_{j\in NN(i)} \boldsymbol{E}_i^{jj} = 4B\boldsymbol{I}, \tag{66}$$

and $mod(\boldsymbol{k}^2)$

$$B \sum_{\substack{j\in NN(i)\\ k\in NN(j)\\ k\neq i}} \boldsymbol{E}_j^{ki} e^{i\boldsymbol{k}\cdot(\boldsymbol{v}_j - \boldsymbol{v}_k)} = \frac{-B}{3}(4\boldsymbol{I} - a^2\boldsymbol{k}\otimes\boldsymbol{k}). \tag{67}$$

The block $\boldsymbol{A}_{UV}$ is ($mod|\boldsymbol{k}|^2$) the sum of

$$A \sum_{j\in NN(i)} \boldsymbol{E}_i^{jj} e^{i\boldsymbol{k}\cdot\boldsymbol{v}_j} = -\frac{4A}{3}\boldsymbol{I} + i\frac{aA}{3}\boldsymbol{S} + a^2\frac{A}{24}\left[\boldsymbol{k}\otimes\boldsymbol{k} + \boldsymbol{S}^2\right] \tag{68}$$

$$B \sum_{\substack{\{j,k\}\subset NN(i)\\ k\neq j}} (\boldsymbol{E}_i^{jj} + \boldsymbol{E}_i^{kj}) e^{i\boldsymbol{k}\cdot\boldsymbol{v}_k} = B \sum_{\substack{\{j,k\}\subset NN(i)\\ k\neq j}} (\boldsymbol{E}_i^{jk} + \boldsymbol{E}_i^{kk}) e^{i\boldsymbol{k}\cdot\boldsymbol{v}_j} =$$

$$= -\frac{8B}{3}\boldsymbol{I} + i\frac{2aB}{3}\boldsymbol{S} + a^2\frac{B}{12}\left[\boldsymbol{k}\otimes\boldsymbol{k} + \boldsymbol{S}^2\right] \tag{69}$$

and

$$B \sum_{\substack{j\in NN(i)\\ k\in NN(j)\\ k\neq i}} (\boldsymbol{E}_j^{kk} + \boldsymbol{E}_j^{ki}) e^{i\boldsymbol{k}\cdot\boldsymbol{v}_j} = \frac{-B}{3}(4\boldsymbol{I} - a^2\boldsymbol{k}\otimes\boldsymbol{k}). \tag{70}$$

As already noted $\boldsymbol{A}_{VV}$ is identical to $\boldsymbol{A}_{UU}$ where vectors $\boldsymbol{v}_i$ are replaced by $-\boldsymbol{v}_i$. Then, a straightforward computation shows that $\boldsymbol{A}_{VV} = \boldsymbol{A}_{UU}$ so that finally, the dispersion matrix is $(mod|\boldsymbol{k}|^2)$

$$\boldsymbol{A}(\boldsymbol{k}) = \begin{bmatrix} \boldsymbol{A}_{UU} & \boldsymbol{A}_{UV} \\ \boldsymbol{A}^{\star}_{UV} & \boldsymbol{A}_{UU} \end{bmatrix} \tag{71}$$

where

$$\begin{aligned} \boldsymbol{A}_{UU} &= \frac{4}{3}(A+4B)\boldsymbol{I} + \frac{a^2 B}{3}\boldsymbol{k}\otimes\boldsymbol{k} && (72) \\ \boldsymbol{A}_{UV} &= (A+4B)(-\frac{4}{3}\boldsymbol{I} + \frac{a^2}{24}\boldsymbol{k}\otimes\boldsymbol{k}) + \frac{iA}{3}(A-4B)\boldsymbol{S} + (A-4B)\frac{a^2}{12}\boldsymbol{P}. && (73) \end{aligned}$$

Separation of acoustical and optical branches is performed by changing to collective variables, i.e. from $(\boldsymbol{U}, \boldsymbol{V})$ to $(\frac{1}{\sqrt{2}}(\boldsymbol{U}+\boldsymbol{V}), \frac{1}{\sqrt{2}}(\boldsymbol{U}-\boldsymbol{V}))$. This leads to

$$\boldsymbol{A} = \begin{pmatrix} \boldsymbol{A}_{aa}(\boldsymbol{k}) & \boldsymbol{A}_{ao}(\boldsymbol{k}) \\ \boldsymbol{A}^{\star}_{ao}(\boldsymbol{k}) & \boldsymbol{A}_{oo}(\boldsymbol{k}) \end{pmatrix}. \tag{74}$$

We have

$$\begin{aligned} \boldsymbol{A}_{aa}(\boldsymbol{k}) &= \frac{1}{12}a^2 A\boldsymbol{P} + \frac{1}{24}a^2(A+4B)(\boldsymbol{k}\cdot\boldsymbol{k})\boldsymbol{I} + \frac{1}{3}a^2 B\boldsymbol{T} && (75) \\ \boldsymbol{A}_{ao}(\boldsymbol{k}) &= \frac{1}{3}a(A-4B)\boldsymbol{S} && (76) \\ \boldsymbol{A}_{oo}(\boldsymbol{k}) &= (\frac{8}{3}(A+4B) - \frac{1}{24}a^2(\boldsymbol{k}\cdot\boldsymbol{k}))\boldsymbol{I} - \frac{1}{12}a^2(A-8B)\boldsymbol{P} + \frac{1}{3}a^3 B\boldsymbol{T}. && (77) \end{aligned}$$

We note that $\boldsymbol{A}_{aa}$, $\boldsymbol{A}_{ao}$ and $\boldsymbol{A}_{oo}$ are respectively $O(|\boldsymbol{k}|^2)$, $O(|\boldsymbol{k}|)$, and $O(1)$. Using relation (32) we are lead to (33).